Effect of Initial Void Shape on the Occurrence of Cavitation Instabilities in Elastic-Plastic Solids

V. Tvergaard
Department of Solid Mechanics,
The Technical University of Denmark,
DK-2800 Lyngby, Denmark

J. W. Hutchinson
Division of Applied Sciences,
Harvard University,
Cambridge, MA 02138
Fellow ASME

A void in an infinite elastic-plastic material grows without bound when a cavitation stress limit is reached. Such unstable void expansion, driven by the elastic energy stored in the surrounding material, has been studied for the relatively simple case of spherically symmetric conditions and also for a spherical void in an axisymmetric remote stress field. The analyses are here extended to consider the effect of a void with an initially prolate or oblate spheroidal shape. Numerical unit cell analyses are carried out for a power-hardening elastic-plastic material subject to various axisymmetric remote stress states. For the range of void shapes analyzed it is found that the critical cavitation stress state shows very little influence of the initial void shape.

1 Introduction

Cavitation instabilities in metals occur under rather rare conditions in which plastic flow is highly constrained leading to mean tensile stress levels which are more than four or five times the tensile flow stress of the solid. Although mean stress levels of that magnitude are seldom achieved, there are some important applications where such levels can occur and for which spontaneous cavitation is a potential failure mechanism. Situations where thin layers of a ductile metal are bonded to phases which are capable of only elastic deformation are likely candidates, as in ceramic particle reinforced metal matrix composites and in layered structures with ceramic layers alternating with metal layers. A striking example of cavitation instabilities was observed by Ashby, Blunt, and Bannister (1989) in tensile experiments on highly constrained ductile wires. In each specimen, a single void ballooned open in the region of highest triaxiality, most likely nucleated at some kind of second phase particle whose size would be measured in microns. These voids increased their volume by more than six orders of magnitude essentially spontaneously when critical conditions were reached. It is in this sense that a cavitation instability should be regarded as a material instability, quite distinct from conventional void growth which takes place incrementally and stably in proportion to imposed overall straining.

Early work on cavitation instabilities is summarized in Hill (1950). The earliest work was confined to either axisymmetric or spherical symmetric voids subject to stress loadings with the same symmetry. Recently these studies have been extended to the case of initially spherical voids under nonspherically symmetric stressing (Huang et al., 1991; Tvergaard et al., 1992; Hou and Abeyaratne, 1992). The critical remote stress states associated with the cavitation instability have been determined for an isolated initially spherical void in an infinite elastic-plastic medium. A somewhat different way of interpreting cavitation instabilities has been promulgated in studies of the phenomenon within the context of nonlinearly elastic solids. Ball (1982) views cavitation as a bifurcation from a homogeneously stressed state by allowing for bifurcation fields which are singular at the point of origin of the void (see Horgan (1992) for further discussion of the two interpretations and for further references to the elasticity literature). This alternative viewpoint lends itself naturally to the labelling of the phenomena as an inherent material instability.

With the exception of the three aforementioned papers, all the studies, whether for elastic or elastic-plastic solids, have been carried out under restrictions of either axial or spherical symmetry. The term material instability suggests that the critical cavitation stress states should not be a function of, for example, the initial shape of the void or, equivalently, of the details of any initial imperfection when viewed within the bifurcation context. This seems to be implicit in much of the literature, but it has not been established. The objective of this paper is to address this issue by determining to what extent, if any, the cavitation stress states are a function of the initial shape of the voids. Specifically, we will present results for an isolated void with an initially prolate or oblate spheroidal shape in an infinite elastic-plastic solid. The solid is subject to general

Contributed by the Applied Mechanics Division of THE AMERICAN SOCIETY OF MECHANICAL ENGINEERS for publication in the ASME JOURNAL OF APPLIED MECHANICS.

Discussion on this paper should be addressed to the Technical Editor, Professor Lewis T. Wheeler, Department of Mechanical Engineering, University of Houston, Houston, TX 77204-4792, and will be accepted until four months after final publication of the paper itself in the ASME JOURNAL OF APPLIED MECHANICS.

Manuscript received by the ASME Applied Mechanics Division, Jan. 20, 1992; final revision, Aug. 17, 1992. Associate Technical Editor: G. J. Dvorak.

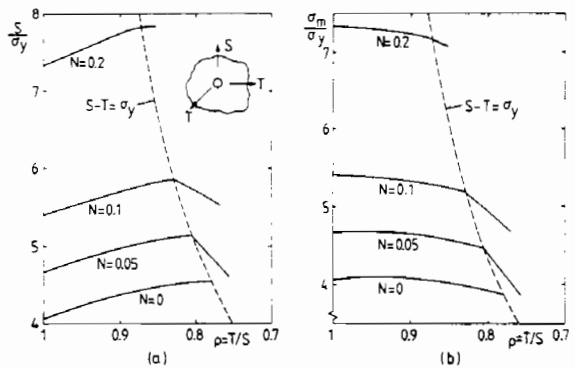

Fig. 1 Cavitation limits for a spherical void in an elastic-plastic power-hardening solid, with $\sigma_y/E = 0.003$ and $\nu = 0.3$; (*a*) axial tensile stress, (*b*) mean stress (from Tvergaard et al., 1992)

combinations of remote stress states sharing a common axis of symmetry with the void.

2 Cavitation in Axisymmetric Stress Field

For an isolated spherical void in an infinite, remotely stressed elastic-perfectly plastic solid the occurrence of cavitation instabilities has been analyzed by Huang et al. (1991), and the analysis was extended to power-hardening elastic-plastic solids by Tvergaard et al. (1992). The remote principal true stresses, leading to an axisymmetric stress state, were taken to be

$$\sigma_1^\infty = S, \quad \sigma_2^\infty = \sigma_3^\infty = T \tag{1}$$

and the analyses focussed on stress states where $S \geq T$. For the special case of a single spherical void in an elastic-plastic material subject to remote pure hydrostatic tension ($S = T$), where spherical symmetries apply, the analysis is relatively simple (Hill, 1950; Huang et al., 1991).

The dependence of the cavitation instability limit on the remote stress ratio T/S is shown in Fig. 1 (Tvergaard et al., 1992) for an elastic-plastic power-hardening material with initial yield stress $\sigma_y/E = 0.003$ and Poisson's ratio $\nu = 0.3$, including the result for an elastic-perfectly plastic solid ($N = 0$). These results for a spherical void include also the special case of spherical symmetry ($S = T$), and it is seen that the critical tensile stress S or mean stress σ_m for cavitation instability is strongly increased by strain hardening.

The solution procedure used by Huang et al. (1991) for general axisymmetric states of deformation is based on coupling an outer solution to a finite element representation of the solution in an inner region. The outer solution is either a purely elastic solution or a purely plastic solution, which consists of a uniform field corresponding to a uniform stress state equal to the remote stresses, with the lowest order perturbation superposed. The inner solution is a full finite strain solution, and the two solutions are coupled by requiring continuity of displacement increments and nominal traction increments across a spherical surface with radius $R = R^*$.

In the present analyses for voids with initial ellipsoidal shapes, it has been preferred to use a finite element approximation in the whole region analyzed. Thus a cylindrical cell model (Fig. 2) with a central void is analyzed. This type of cell model has been used previously (Tvergaard, 1982; Hutchinson and Tvergaard, 1989) to represent a periodic distribution of voids; but in the present computations, very low void volume fractions of about $2.5 \cdot 10^{-11}$ are considered so that the studies give a good approximation of the behavior of a single void in an infinite solid. The cell model analysis gives an accurate representation of the stress history in the material near the void, since the void surface is load free throughout the deformations. By contrast, in the analyses based on coupling an inner solution to an outer solution (Huang et al., 1991; Tvergaard et al., 1992), an initial uniform stress state is enforced by applying void surface loads, which are subsequently stepped down; but this gives a somewhat inaccurate stress history in the material near the void, which may result in an inaccuracy of the path-dependent elastic-plastic solution.

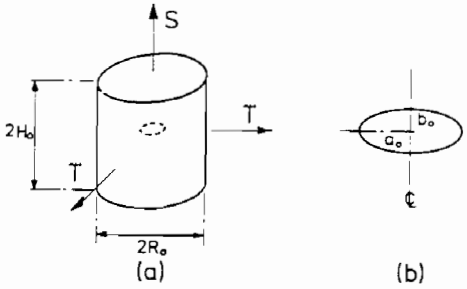

Fig. 2 (*a*) Cylindrical cell model used to analyze cavitation; (*b*) initial void shape

The cylindrical unit cell has the initial radius R_0 and height $2H_0$ (Fig. 2). Due to symmetry about the middle plane, only half of the cell needs to be analyzed. The void at the center of the cell is taken to be ellipsoidal, with initial half-axes a_0 and b_0 in the radial and axial directions, respectively. A cylindrical reference coordinate system is used, in which x^1 is the axial coordinate, x^2 is the radial coordinate, and x^3 is the circumferential angle. In terms of the displacement components u^i on the reference base vectors and the nominal surface tractions T^i, the boundary conditions for the unit cell are, on incremental form,

$$\dot{u}^1 = 0, \quad \dot{T}^2 = \dot{T}^3 = 0, \quad \text{at } x^1 = 0 \tag{2}$$

$$\dot{u}^1 = \dot{U}_I, \quad \dot{T}^2 = \dot{T}^3 = 0, \quad \text{at } x^1 = H_0 \tag{3}$$

$$\dot{u}^2 = \dot{U}_{II}, \quad \dot{T}^1 = \dot{T}^3 = 0, \quad \text{at } x^2 = R_0 \tag{4}$$

$$\dot{T}^i = 0, \quad \text{at } \left(\frac{x^1}{b_0}\right)^2 + \left(\frac{x^2}{a_0}\right)^2 = 1. \tag{5}$$

The two constants $\dot{U}_I$ and $\dot{U}_{II}$ are displacement increments and the ratio $\dot{U}_{II}/\dot{U}_I$ is calculated in each increment such that there is a fixed prescribed ratio, $\rho = T/S$, between the macroscopic true stresses (see Tvergaard, 1982).

Constitutive relations and equilibrium equations are given here in the context of a convected coordinate formulation of the field equations. The Lagrangian strain tensor is expressed in terms of the displacement components as

$$\eta_{ij} = \frac{1}{2}\left(u_{i,j} + u_{j,i} + u^k_{,i} u_{k,j}\right) \tag{6}$$

where $(\ )_{,j}$ denotes covariant differentiation in the reference frame, indices range from one to three, and the summation convention is adopted for repeated indices. The contravariant components of the Kirchhoff stress tensor τ^{ij} and the Cauchy stress tensor σ^{ij} are related by

$$\tau^{ij} = \sqrt{G/g}\ \sigma^{ij} \tag{7}$$

where g and G are the determinants for the metric tensors g_{ij} and G_{ij} in the reference configuration and the current configuration, respectively.

The elastic-plastic material behavior is represented by a finite strain generalization of J_2 flow theory (Hutchinson, 1973). The incremental stress-strain relationship is of the form $\dot{\tau}^{ij} = L^{ijkl}\,\dot{\eta}_{kl}$, with the tensor of instantaneous moduli given by

$$L^{ijkl}=\frac{E}{1+\nu}\left\{\frac{1}{2}\left(G^{ik}G^{jl}+G^{il}G^{jk}\right)+\frac{\nu}{1-2\nu}G^{ij}G^{kl}\right.$$
$$\left.-\beta\frac{3}{2}\frac{E/E_t-1}{E/E_t-(1-2\nu)/3}\frac{s^{ij}s^{kl}}{\sigma_y^2}\right\}$$
$$-\frac{1}{2}\left(G^{ik}\tau^{jl}+G^{il}\tau^{jk}+G^{jl}\tau^{ik}+G^{jk}\tau^{il}\right) \quad (8)$$

$$\beta=\begin{cases}1, & \text{for } \sigma_e=(\sigma_e)_{\max} \text{ and } \dot{\sigma}_e\geq 0\\ 0, & \text{for } \sigma_e<(\sigma_e)_{\max} \text{ or } \dot{\sigma}_e<0.\end{cases} \quad (9)$$

Here $\sigma_e = (3s_{ij}s^{ij}/2)^{1/2}$ is the effective Mises stress, $s^{ij} = \tau^{ij} - G^{ij}\tau^k_k/3$ is the stress deviator tensor, E is Young's modulus, and ν is Poisson's ratio. The tangent modulus E_t is the slope of the uniaxial true stress versus natural strain curve, which is here represented by a piecewise power law

$$\epsilon=\begin{cases}\dfrac{\sigma}{E}, & \text{for } \sigma\leq\sigma_y\\ \dfrac{\sigma_y}{E}\left(\dfrac{\sigma}{\sigma_y}\right)^{1/N}, & \text{for } \sigma>\sigma_y.\end{cases} \quad (10)$$

The finite strain generalization of J_2 flow theory employed here is formulated directly in terms of Kirchhoff stresses rather than Cauchy stresses (see Hutchinson, 1973), and thus the value of the effective Mises stress σ_e used in (8) and (9) is $\sqrt{G/g}$ times the corresponding effective stress value Σ_e defined in terms of Cauchy stresses. This difference is small, since G/g differs from unity only due to elastic compressibility.

3 Numerical Method

The equations of equilibrium are expressed in terms of the principle of virtual work, and a numerical solution is obtained by a linear incremental solution procedure. The equations governing the stress increments $\Delta\tau^{ij}$, the strain increments $\Delta\eta_{ij}$, etc., are obtained by expanding the principle of virtual work about the current state, using (6). To lowest order the incremental equation is

$$\int_V\left\{\Delta\tau^{ij}\delta\eta_{ij}+\tau^{ij}\Delta u^k_{,i}\delta u_{k,j}\right\}dV$$
$$=\int_A\Delta T^i\delta u_i dA-\left[\int_V\tau^{ij}\delta\eta_{ij}dV-\int_A T^i\delta u_i dA\right] \quad (11)$$

where V and A are the volume and surface, respectively, of the body in the reference configuration, and T^i are contravariant components of the nominal surface tractions. The bracketed terms are included to prevent drifting of the solution away from the true equilibrium path.

The meshes used in the incremental finite element solutions consists of quadrilaterals, each built up of four triangular, linear displacement elements. The integrals in (11) are evaluated at one central point within each element. An example of a mesh used for the analyses is shown in Fig. 3, illustrating both the outer mesh in the half unit cell analyzed and the central part of the mesh near a void with $a_0/b_0 = 4$.

A special Rayleigh-Ritz finite element method (Tvergaard, 1976) is used to be able to prescribe a node displacement at the void surface rather than the end displacement U_I without applying a load on the void surface. This improves the numerical stability near the occurrence of a cavitation instability where $\dot{U}_i \to 0$.

The average straining of the void is determined from the

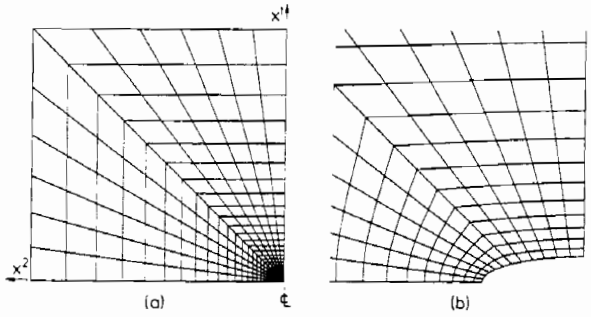

Fig. 3 Mesh used for numerical analyses; (*a*) outer mesh in half-unit cell, (*b*) inner mesh near a void with $a_0/b_0 = 4$

average displacement gradients F_{ij}, referring to a Cartesian frame, which are calculated as

$$F_{ij}=\delta_{ij}+\frac{1}{V}\int_A u_i n_j dA. \quad (12)$$

Here δ_{ij} is the Kronecker delta, V and A are the volume and surface, respectively, in the reference frame, and u_i and n_j are the Cartesian components of the displacements and the outward unit normal. The axial and transverse components of the gradient, F_{11} and $F_{22} = F_{33}$, respectively, are then used to define average half-axes a and b of the deformed void, such that

$$a=F_{22}a_0,\ b=F_{11}b_0. \quad (13)$$

Based on these average half-axes, the development of the ratio a/b will be used to illustrate the void shape changes during growth.

4 Results

The analyses to be presented here are carried out for a power-hardening material with $N = 0.1$ and $\sigma_y/E = 0.003$, and the value of Poisson's ratio is taken to be $\nu = 0.3$. Furthermore, the ratio of the average true stresses, $\rho = T/S$, is kept constant in each case studied, and thus the results to be presented are directly comparable with the curve for $N = 0.1$ shown in Fig. 1, obtained by Tvergaard et al. (1992) for initially spherical voids.

Figure 4 shows results obtained for remote hydrostatic tension, $T/S = 1$. Thus here the stress and strain fields far from the void satisfy conditions of spherical symmetry, as is directly shown by the numerical solutions, but near the voids spherical symmetry breaks down, and general axisymmetric fields develop due to the ellipsoidal initial void shapes.

As a measure of the void dilatation rate the development of $\dot{V}/(\dot{\epsilon}_1 V)$ is shown in Fig. 4(*a*), normalized by its value at $V/V_0 = 2$. Here, V_0 and V are the initial and current void volumes, respectively, and $\epsilon_1 = \ln(1 + U_1/H_0)$ denotes the average logarithmic strain in the x^1-direction. For $S \geq T$, where $\dot{\epsilon}_1 > 0$ if $\dot{S} > 0$, the occurrence of a cavitation state is determined by the condition that $\dot{V}/(\dot{\epsilon}_1 V)$ is unbounded as the stress state is approached from below. This is clearly illustrated by the plot of the normalized dilatation rate versus V/V_0 in Fig. 4(*a*), which shows that $\dot{V}/(\dot{\epsilon}_1 V)$ grows rapidly as the void volume increases. The occurrence of cavitation instabilities in this case of remote hydrostatic tension is also illustrated by the fact that the slope becomes zero for the curves of S/σ_y versus V/V_0 in Fig. 4(*c*). It is noted that the numerical stability of the computations decays as the void volume grows very large, leading to a strongly distorted mesh. Therefore, the predicted dilatation rates $\dot{V}/(\dot{\epsilon}_1 V)$ start to oscillate at the end of the computations shown in Fig. 4 after the stage illustrated by the curves in Fig. 4(*a*).

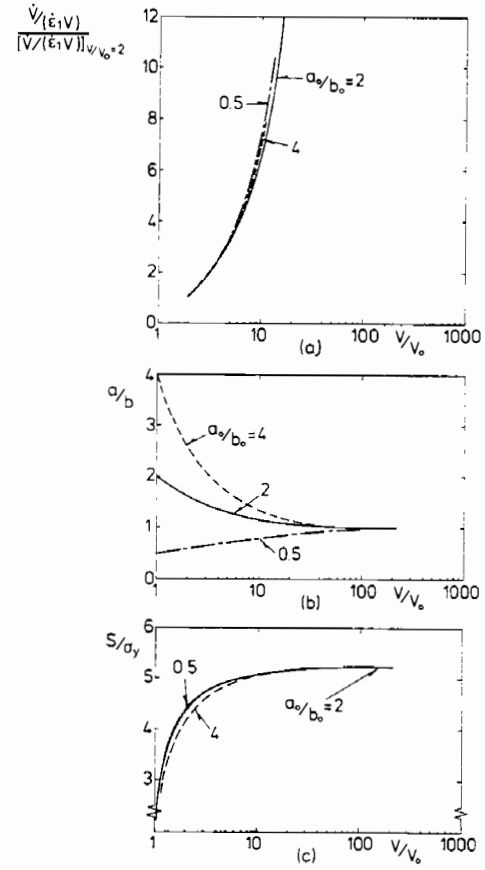

Fig. 4 Cavitation behavior versus void volume, for $T/S = 1$; (*a*) normalized dilatation rate, (*b*) void shape, (*c*) remote axial stress

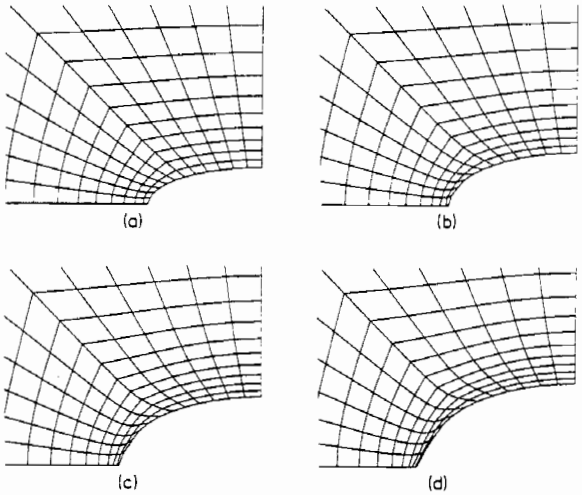

Fig. 5 Deformed inner meshes for $a_0/b_0 = 4$ and $T/S = 1$; (*a*) $V/V_0 = 1.70$, (*b*) $V/V_0 = 2.98$, (*c*) $V/V_0 = 4.67$, (*d*) $V/V_0 = 6.81$

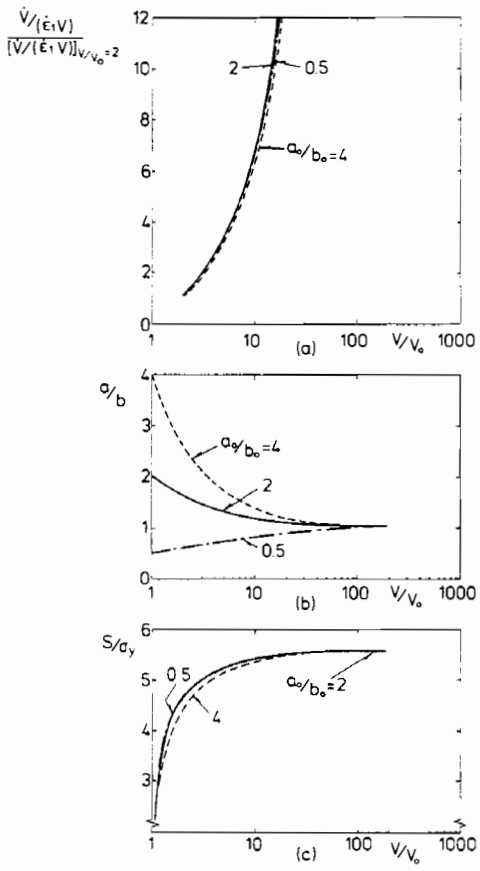

Fig. 6 Cavitation behavior versus void volume, for $T/S = 0.9$; (*a*) normalized dilatation rate, (*b*) void shape, (*c*) remote axial stress

The development of the void shape for increasing volume is illustrated by the curves of a/b versus V/V_0 in Fig. 4(*b*). Computations have been carried out for three different ellipsoidal shapes, $a_0/b_0 = 4$, $a_0/b_0 = 2$, and $a_0/b_0 = 0.5$, and it is seen that in all three cases the ratio a/b grows very close to unity, indicating that the growing voids become nearly spherical. Also, more extreme void shapes, $a_0/b_0 = 0.25$ and $a_0/b_0 = 6$, have been analyzed; but these computations break down numerically at an earlier stage than those shown in Fig. 4, due to strongly distorted meshes. Although these additional computations are not included in Fig. 4, it is noted that the trends are the same as those shown in the figure.

Both a circular cylindrical void and a spherical void were analyzed by Tvergaard et al. (1992), and it was found that the critical stress for cavitation instability is significantly lower in the case of a cylindrical void. Thus for the material considered here, with $N = 0.1$, $\sigma_y/E = 0.003$ and $\nu = 0.3$, the critical cavitation instability stress is 15 percent lower for a cylindrical void than that corresponding to a spherical void. In the case of ellipsoidal voids the behavior should approach that of cylindrical voids for very small values of a_0/b_0, but this tendency is not visible in Fig. 4(*c*). In fact, the cavitation instability stress found for $a_0/b_0 = 0.5$ is slightly smaller than that found for $a_0/b_0 = 4$, as expected, but the difference is only 0.4 percent. To obtain a cavitation instability stress closer to that for cylindrical voids, it is expected that the ratio a_0/b_0 would have to be so small that the void is still cylinder like when it has grown so large that the cavitation instability stress is approached.

Examples of mesh deformations near the void are shown in Fig. 5 for the case $a_0/b_0 = 4$, with $T/S = 1$, also illustrated in Fig. 4. These four deformed meshes correspond to rather early stages, at the values 1.70, 2.98, 4.67, and 6.81 of V/V_0; but it is seen from the corresponding curve in Fig. 4(*b*) that most of the void shape change takes place at this early stage. The elements around the void circumference are already strongly deformed in Fig. 5(*d*), since large strains develop in this region where the void surface was initially most strongly curved, and this is also the region where the most pronounced mesh distortions develop later on.

As the stress level approaches the cavitation instability limit, the strains grow very large at the void surface, and there is the

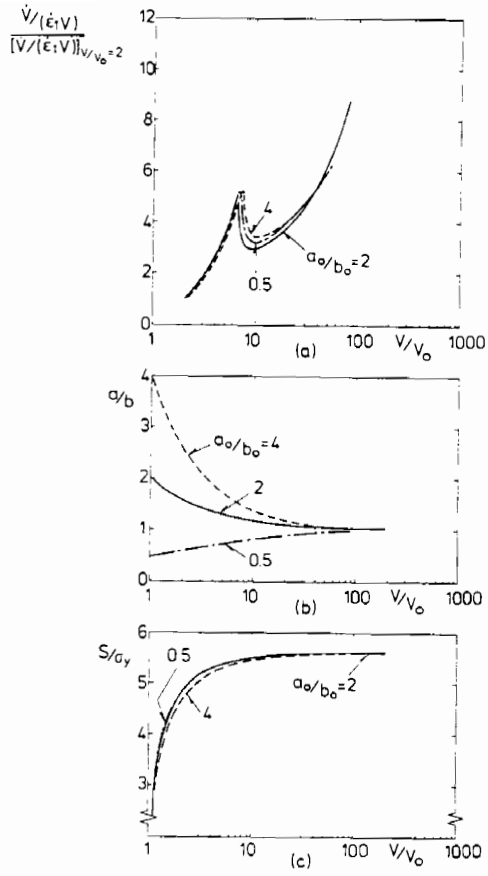

Fig. 7 Cavitation behavior versus void volume, for $T/S = 0.82$; (*a*) normalized dilatation rate, (*b*) void shape, (*c*) remote axial stress

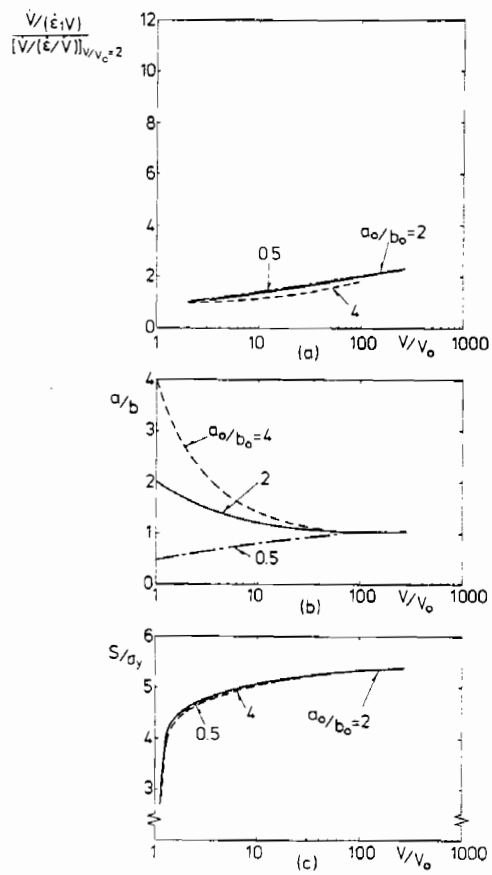

Fig. 8 Cavitation behavior versus void volume, for $T/S = 0.78$; (*a*) normalized dilatation rate, (*b*) void shape, (*c*) remote axial stress

possibility that bifurcation into a short wave surface instability takes place (see Hutchinson and Tvergaard, 1980). In the present computations the solid is characterized by the J_2 flow theory for which the surface wave bifurcation strain is essentially unattainable (apart from the special case of a very low-hardening material under plane-strain conditions). Thus in the present analyses, as well as the J_2 flow theory analyses of Huang et al. (1991) and Tvergaard et al. (1992), the occurrence of a surface instability prior to the cavitation instability is not likely. However, in analyses based on deformation theory (Hou and Abeyaratne, 1992; Tvergaard et al., 1992) the critical strains for surface instabilities and shear bands are not so large, and here the interaction with such modes of instability in the material near the void surface may have to be accounted in an accurate analysis of cavitation instabilities.

Computations have also been carried out for a remote axisymmetric stress state, $T/S = 0.9$, as illustrated in Fig. 6. As in Fig. 4, the normalized dilatation rate $\dot{V}/(\dot{\epsilon}_1 V)$ grows large at a rather early stage, indicating that a cavitation state will be reached, and this is also seen by the vanishing shape at the ends of the curves for S/σ_y versus V/V_0 in Fig. 6(*c*). Furthermore, it is noted from Fig. 6(*c*) that the limiting value of S/σ_y is larger for $T/S = 0.9$ than found in Fig. 4(*c*) for $T/S = 1$, in agreement with the results of Tvergaard et al. (1992) for initially spherical voids (see Fig. 1). Also the $T/S = 0.9$ the voids grow into a nearly spherical shape, as is seen from Fig. 6(*b*).

A common feature of the two cases $T/S = 1$ and $T/S = 0.9$ considered in Figs. 4 to 6 is that the fields far from the voids remain elastic (see also Fig. 1). For all cases in which the remote fields remain elastic Tvergaard et al. (1992) found that a cavitation state is reached, but in cases where remote plastic yielding occurs the conclusions were less clear. For an initially spherical void in a strain-hardening elastic-plastic solid, the results did indicate the occurrence of a cavitation instability under remote plastic yielding. However, for a circular cylindrical void the occurrence of an instability seemed more uncertain, even though a cavitation state was clearly predicted for the corresponding deformation theory solid, i.e., a nonlinear elastic solid (Tvergaard et al., 1992).

Figure 7 shows results for $T/S = 0.82$, which is just beyond the limit where remote yielding occurs for the material analyzed here. In this case the development of the normalized dilatation rate (Fig. 7(*a*)) differs significantly from that found in the previous two cases. Initially, the growth of $\dot{V}/(\dot{\epsilon}_1 V)$ is very similar to the results shown in Fig. 4(*a*) and 6(*a*); but then at $V/V_0 \simeq 7$, where plastic yielding initiates in regions far from the void, the normalized dilatation rates decay sharply. Subsequently, as plastic yielding continues in the outer regions of the circular cylindrical cell analyzed, $\dot{V}/(\dot{\epsilon}_1 V)$ starts to grow strongly again, and Fig. 7(*a*) as well as the vanishing slope at the ends of the curves in Fig. 7(*c*) indicate that a cavitation state will be reached for $T/S = 0.82$ during remote plastic yielding. Figure 7(*b*) shows that also in this stress state the initially ellipsoidal voids develop into near spherical shapes as they grow large.

For $T/S = 0.78$, plastic yielding in the remote fields occurs even earlier (Fig. 8). Thus remote yielding sets in at $V/V_0 < 2$ prior to the start of the curves in Fig. 8(*a*) so that these curves do not show a local maximum as that found in Fig. 7(*a*). Furthermore, the growth of the normalized dilatation rate $\dot{V}/(\dot{\epsilon}_1 V)$ as a function of V/V_0 is slow in Fig. 8(*a*), and the curves in Fig. 8(*c*) have clearly not yet reached a horizontal asymptote at the points where the computations are stopped due to numerical instabilities induced by a strongly distorted

mesh. Thus based on the computations illustrated in Fig. 8 it is not possible to conclude that a cavitation state will be reached in the J_2 flow theory solid for $T/S = 0.78$. A cavitation state may very well be reached at a later stage, but the curves in Fig. 8 indicate that the computations would have to be continued to values of V/V_0 much larger than 200 in order to approach a possible cavitation state.

5 Conclusions

The numerical results reported above demonstrate quite convincingly that, within the range of stress states for which cavitation occurs, the critical stresses themselves are virtually independent of the shape of the initial void. We suspect that the very small differences which have been computed (typically less than half a percent) are partly a consequence of numerical discretization. It has also been demonstrated that the cavitation stress states for infinitely long cylindrical voids, which are attained prior to those for finite aspect ratio voids, are not approaches for voids starting as prolate spheroids with aspect ratio less than about four ($a_0/b_0 > 0.25$). It remains an open question as to how large an aspect ratio would be required to reach a transition to the cylindrical cavitation states.

Acknowledgment

The work of JWH was supported in part by the National Science Foundation (Grant NSF-MSS-90-20141) and by the Division of Applied Sciences, Harvard University.

References

Ashby, M. F., Blunt, F. J., and Bannister, M., 1989, "Flow Characteristics of Highly Constrained Metal Wires," *Acta Metallurgica*, Vol. 37, pp. 1847–1857.

Ball, J. M., 1982, "Discontinuous Equilibrium Solutions and Cavitation in Nonlinear Elasticity," *Phil. Trans. R. Soc. Lond.*, Vol. A306, pp. 557–610.

Hill, R., 1950, *The Mathematical Theory of Plasticity*, Clarendon Press, Oxford, UK.

Horgan, C. O., 1992, "Void Nucleation and Growth for Compressible Nonlinearly Elastic Materials: an Example," *Int. J. Solids Structures*, Vol. 29, pp. 279–291.

Hou, H.-S., and Abeyaratne, R., 1992, "Cavitation in Elastic and Elastic-Plastic Solids," *J. Mech. Phys. Solids*, Vol. 40, pp. 571–592.

Huang, Y., Hutchinson, J. W., and Tvergaard, V., 1991, "Cavitation Instabilities in Elastic-Plastic Solids," *J. Mech. Phys. Solids*, Vol. 39, pp. 223–241.

Hutchinson, J. W., 1973, "Finite Strain Analysis of Elastic-Plastic Solids and Structures," *Numerical Solution of Nonlinear Structural Problems*, R. F. Hartung, ed., Vol. 17, ASME, New York.

Hutchinson, J. W., and Tvergaard, V., 1980, "Surface Instabilities on Statically Strained Plastic Solids," *Int. J. Mech. Sci.*, Vol. 22, pp. 339–354.

Hutchinson, J. W., and Tvergaard, V., 1989, "Softening Due to Void Nucleation in Metals," *Fracture Mechanics: Perspective and Directions*, ASTM STP 1020, R. P. Wei and R. P. Gongloff, eds., American Society for Testing and Materials, Philadelphia, pp. 61–83.

Tvergaard, V., 1976, "Effect of Thickness Inhomogeneities in Internally Pressurized Elastic-Plastic Spherical Shells," *J. Mech. Phys. Solids*, Vol. 24, pp. 291–304.

Tvergaard, V., 1982, "On Localization in Ductile Materials Containing Spherical Voids," *Int. J. Fracture*, Vol. 18, pp. 237–252.

Tvergaard, V., Huang, Y., and Hutchinson, J. W., 1992, "Cavitation Instabilities in a Power Hardening Elastic-Plastic Solid," *Eur. J. Mech. A/Solids*, Vol. 11, pp. 215–231.